Journal of Physics B: Atomic, Molecular and Optical Physics

Tomographic entanglement indicators in frequency combs and Talbot carpets

OPEN ACCESS
IOP Publishing
Journal of Physics B: Atomic, Molecular and Optical Physics
J. Phys. B: At. Mol. Opt. Phys. **55** (2022) 185501 (9pp)
https://doi.org/10.1088/1361-6455/ac870d

Tomographic entanglement indicators in frequency combs and Talbot carpets

B Sharmila[*,1], **S Lakshmibala and V Balakrishnan**

Department of Physics, Indian Institute of Technology Madras, Chennai 600036, India

E-mail: Sharmila.Balamurugan@warwick.ac.uk

Received 27 November 2021, revised 27 July 2022
Accepted for publication 3 August 2022
Published 23 August 2022

Abstract

Recent theoretical investigations on tomographic entanglement indicators have showcased the advantages of the tomographic approach in the context of continuous-variable (CV), spin and hybrid quantum systems. Direct estimation of entanglement using experimental data from the IBM quantum computing platform and NMR experiments has also been carried out in earlier work. A similar investigation in the context of CV systems is necessary to assess fully the utility of the tomographic approach. In this paper, we highlight the advantages of this approach in the context of experiments reported in the literature on two CV systems, namely, entangled Talbot carpets and entangled biphoton frequency combs. We use the tomographic entanglement indicator to estimate the degree of entanglement between a pair of Talbot carpets, and demonstrate that this provides a simpler and more direct procedure as compared to the one suggested in the experiment. We also establish that the tomograms corresponding to two biphoton frequency combs carry clear entanglement signatures that distinguish between the two states.

Keywords: quantum entanglement, tomograms, tomographic entanglement indicator, Talbot carpet, biphoton frequency comb

(Some figures may appear in colour only in the online journal)

1. Introduction

The measurement of any observable in a quantum mechanical system yields a histogram of the state of the system in the eigenbasis of that observable. Measurements of a judiciously chosen *quorum* of appropriate observables of a system that are informationally complete yield a set of histograms called a tomogram. Quantum state reconstruction seeks to obtain the density matrix from the tomogram. However, the reconstruction of the state of a radiation field from the corresponding optical tomogram could be both tedious and complex [1]. In many contexts, the reconstruction program is also limited by the presence of inherent aberrations in the source [2, 3]. It is worth noting that, even in the simple case of a two-level atom interacting with a radiation field, the state of the field subsystem was experimentally reconstructed from the corresponding tomogram at various instants during temporal evolution only as recently as 2017 [4]. With an increase in the number of field modes interacting with an atomic system, the inevitable entanglement that arises during dynamical evolution makes state reconstruction an increasingly formidable task. It would therefore be very helpful to *read off* information about a state, wherever possible, directly from the experimentally accessible histograms. In particular, estimating the extent of entanglement through simple manipulations of the relevant tomograms *alone* becomes an interesting and important exercise.

Entanglement is an essential resource in quantum information processing, and quantifying the entanglement between two subsystems of a bipartite system is necessary for this purpose. One of the standard measures of entanglement between

* Author to whom any correspondence should be addressed.
[1] Present address: Department of Physics, University of Warwick, Coventry CV4 7AL, United Kingdom.

the two subsystems A and B of a bipartite system is the subsystem von Neumann entropy $\xi_{\rm SVNE} = -{\rm Tr}\,(\rho_i \log_2 \rho_i)$ where ρ_i $(i = {\rm A}, {\rm B})$ is the reduced density matrix of the subsystem concerned. The computation of $\xi_{\rm SVNE}$, however, requires a knowledge of the full density matrix, in contrast to the tomographic approach. The advantage of the latter approach has been illustrated in certain continuous-variable (CV) systems—for instance, in identifying qualitative signatures of entanglement between the radiation fields in the output ports of a quantum beam-splitter [5]. Further, a detailed analysis of entanglement has been carried out theoretically using several indicators obtained directly from tomograms in different contexts, e.g., close to avoided energy-level crossings [6]. The efficacy of such indicators has been assessed by comparison with standard entanglement measures [7, 8]. Further, these indicators have also been examined using the IBM quantum computing platform, by translating certain multipartite hybrid quantum systems into suitable equivalent circuits [9]. It is to be noted that, in these examples, measurements of multiple observables corresponding to the rotated quadrature operators

$$X_\theta = (a{\rm e}^{-{\rm i}\theta} + a^\dagger {\rm e}^{{\rm i}\theta})/\sqrt{2}, \tag{1}$$

(where $(a, a^\dagger)$ are the photon annihilation and creation operators and $\theta \in [0, \pi)$) are required, in principle.

In marked contrast, a different entanglement indicator has been used in certain recent experiments reported in the literature. In an experiment [10] involving an entangled pair of Talbot carpets generated from photons produced from spontaneous parametric down conversion (SPDC), an entanglement indicator $I_{\rm D}$ based on Bell-type inequalities has been used. The Talbot effect itself has been observed in several experimental settings since its discovery in 1836 [11]. In the quantum context, this effect has been demonstrated both with single photons and with entangled photon pairs [12], and also with single photons prepared in a lattice of angular momentum states [13]. Using a four-level quantum dot molecule, the re-formation of a plane wave into a periodic wave-form has been demonstrated [14]. Single photon interference owing to passage through a grating has been invoked to propose the creation of D-dimensional quantum systems encoded in the spatial degrees of freedom of light [15]. A proposal to realise a class of entangled states to demonstrate nonlocality in phase space using grating techniques [16], and the observation of the optical spatiotemporal Talbot effect [17], are further instances of continuing work on the Talbot effect for testing fundamental concepts and implementing quantum information processing.

Another interesting example of interferometry [18] pertains to biphoton frequency combs. Qubits are encoded in this CV system using the time–frequency continuous degrees of freedom of photon pairs generated through the SPDC process. In an attempt to provide higher capacity and increased noise resilience in quantum communication and computations in CV systems with time–frequency entanglement, a biphoton frequency comb with the potential to create a large Hilbert space (648 dimensions) has been investigated [19]. This approach provides a good platform, in principle, for improved quantum communication. The appearance of polarization-entangled biphoton frequency combs with over 1400 frequency modes has been demonstrated experimentally [20]. Such massive mode-entangled biphoton frequency combs are expected to increase the capacity and rate of quantum communication. Protocols have been proposed, involving measurements of appropriate modular variables, that facilitate a read-out of the encoded discrete quantum information from the corresponding logical states. Further, their experimental feasibility has also been discussed [21]. In reference [22], the authors assess the metrological power of different classes of biphoton states with a non-Gaussian time–frequency spectral distribution. These states could possibly be produced with atomic photon sources, bulk nonlinear crystals and integrated photonic waveguide devices. Further, new methods to characterize the spectral-temporal distribution of single photons have been examined in [23]. In reference [24], the authors investigate the interferometric signatures of different spectral symmetries of biphoton states. A sizable literature exists on the generation and manipulation of quantum states of light in nonlinear AlGaAs chips and their use in quantum networks. In particular, the control and the temporal delay between the photons comprising a pair provides a means of switching from symmetric to anti-symmetric quantum frequency states [25]. Quantum state engineering with biphoton states produced by SPDC, and the characterization of arbitrary states with frequency and time degrees of freedom, have been carried out in [26]. A second quantized description treating time and frequency as operators that can be used to define a universal set of gates, and to implement continuous variable quantum information protocols, has been examined in detail [27]. The frequency entanglement of biphoton states has been shown to simulate anyonic particle statistics [28]. Such photon pairs have been studied extensively to investigate entanglement properties and potential logic gate operations [29, 30].

In some of these experiments (see, for instance, [10, 18]), the tomographic approach mentioned earlier provides an efficient, readily usable procedure for capturing signatures of bipartite entanglement and understanding its qualitative features. It has been demonstrated recently [31] that it is possible to implement single-qudit logic gate operations using the Talbot effect. The next step would be to extend this investigation to the case of a pair of entangled Talbot carpets generated using a suitable combination of two such experimental setups. It is here that the tomographic approach comes into its own, as it has the advantage of simplifying considerably the necessary experimental arrangement. Further, we demonstrate the convenience and usefulness of the tomographic indicators in both the experimental situations under discussion, involving, respectively, entangled Talbot carpets and biphoton frequency combs. The versatility of the tomographic approach is brought out by the fact that optical tomograms are useful in the experiment on entangled Talbot carpets, while chronocyclic tomograms display the features of entanglement in the experiment on biphoton frequency combs.

The plan of the rest of this paper is as follows. In section 2, we review the salient features of the relevant tomograms, and describe the entanglement indicators that can be obtained directly from these tomograms. In section 3, we apply our procedure to assess the degree of entanglement between a

pair of Talbot carpets. Whereas it has been suggested in [10] that an experimental setup which uses Bell-type inequalities could determine the degree of entanglement, we demonstrate that tomograms provide a simpler and more direct procedure for this purpose. Further, in section 4, we establish that the respective chronocyclic tomograms corresponding to the two biphoton states provide manifest entanglement signatures that distinguish between the states. Relevant technical details about the two biphoton states are presented in the appendices A and B. We conclude with some brief remarks in the final section.

2. Tomograms

2.1. Quadrature histograms

We begin by describing the salient features of optical tomograms. In a two-mode CV system, the infinite set of rotated quadrature operators [32–34] given by

$$\begin{aligned}\mathbb{X}_{\theta_A} &= (a^\dagger \mathrm{e}^{\mathrm{i}\theta_A} + a\mathrm{e}^{-\mathrm{i}\theta_A})/\sqrt{2}, \quad \text{and}\\ \mathbb{X}_{\theta_B} &= (b^\dagger \mathrm{e}^{\mathrm{i}\theta_B} + b\mathrm{e}^{-\mathrm{i}\theta_B})/\sqrt{2},\end{aligned} \tag{2}$$

(where $\theta_a, \theta_b \in [0, \pi)$) constitute the quorum of observables that carries complete information about the state. Here $(a, a^\dagger)$ and $(b, b^\dagger)$ are the annihilation and creation operators corresponding respectively to subsystems A and B of the bipartite system, so that $[a, a^\dagger] = 1$ and $[b, b^\dagger] = 1$. The bipartite tomogram is

$$w(X_{\theta_A}, \theta_A; X_{\theta_B}, \theta_B) = \langle X_{\theta_A}, \theta_A; X_{\theta_B}, \theta_B|\rho_{\mathrm{AB}}|X_{\theta_A}, \theta_A; X_{\theta_B}, \theta_B\rangle, \tag{3}$$

where ρ_{AB} is the bipartite density matrix and $\mathbb{X}_{\theta_i}|X_{\theta_i}, \theta_i\rangle = X_{\theta_i}|X_{\theta_i}, \theta_i\rangle$ $(i = \mathrm{A}, \mathrm{B})$. Here, $|X_{\theta_A}, \theta_A; X_{\theta_B}, \theta_B\rangle$ stands for $|X_{\theta_A}, \theta_A\rangle \otimes |X_{\theta_B}, \theta_B\rangle$. The normalisation condition is given by

$$\int_{-\infty}^{\infty} \mathrm{d}X_{\theta_A} \int_{-\infty}^{\infty} \mathrm{d}X_{\theta_B} w(X_{\theta_A}, \theta_A; X_{\theta_B}, \theta_B) = 1 \tag{4}$$

for each θ_a and θ_b. We note that $\theta_a = \theta_b = 0$ corresponds to the position quadrature. Since the investigation of entanglement in reference [10] only pertains to the intensity pattern on the screen, we have treated the screen as the tomographic slice. This sets the specific values of θ_a and θ_b equal to zero. As we are only interested in the corresponding slice of the tomogram, we adopt the following simplified notation. A slice of the tomogram (equivalently, the histogram in the position basis) for a bipartite state $|\psi_{\mathrm{AB}}\rangle$ is given by

$$w(x_{\mathrm{A}}; x_{\mathrm{B}}) = |\langle x_{\mathrm{A}}; x_{\mathrm{B}}|\psi_{\mathrm{AB}}\rangle|^2. \tag{5}$$

Here, $\{|\mathrm{x_i}\rangle\}$ $(i = a, b)$ are the position eigenstates in the two subsystems, and $|x_{\mathrm{A}};\ x_{\mathrm{B}}\rangle$ denotes the corresponding product state. The marginal distributions obtained from the joint distribution above yield the corresponding slices $w_{\mathrm{A}}(x_{\mathrm{A}})$ and $w_{\mathrm{B}}(x_{\mathrm{B}})$ of the subsystem (or reduced) tomograms.

2.2. Chronocyclic tomogram

The analogy between an ultrashort light pulse and a quantum mechanical wave function leads [35] to a *chronocyclic* representation for the study of ultrashort pulses, where the time t and frequency ω are the conjugate observables. The state of a single photon of frequency ω is denoted in a spectral representation of infinitely narrow-band pulses by $|\omega\rangle$. The superposed state of a photon that has a frequency ω with a probability amplitude $\mathcal{S}(\omega)$ is given by $\int \mathrm{d}\omega\, \mathcal{S}(\omega)|\omega\rangle$. In an equivalent temporal representation of infinitely short-duration pulses $\{|t\rangle\}$, this one-photon state is $\int \mathrm{d}t\, \widetilde{\mathcal{S}}(t)|t\rangle$, where $\widetilde{\mathcal{S}}(t)$ is the Fourier transform of $\mathcal{S}(\omega)$. A family of rotated observables $(\omega\cos\theta + t\sin\theta)$ can then be defined [36], where ω and t have been scaled by a natural time scale of the system to make them dimensionless. Measurements of these rotated observables form the basis of chronocyclic tomography, in which the set of histograms corresponding to these observables gives the tomogram of the state of a one-photon system. In this chronocyclic representation, a one-photon state can also be described in the time–frequency 'phase space' by a corresponding Wigner function [35]. Extension to multipartite states corresponding to two or more photons is straightforward. For instance, two photons of frequencies ω and ω' are given by the biphoton CV bipartite state $|\omega\rangle \otimes |\omega'\rangle$.

In reference [18], the experiment on biphoton frequency combs is carried out in the time–frequency domain. It follows naturally that, in the tomographic approach, chronocyclic tomograms need to be examined. This allows for four choices of tomographic slices, namely, frequency–frequency, frequency–time, time–frequency, and time–time. We have examined the various possibilities and found that the time–time tomographic slice corresponding to each biphoton entangled state is optimal for distinguishing between them. We note that *a priori* there is no set procedure in general for choosing the optimal slice (i.e., the analogues of θ_{A} and θ_{B} in quadrature tomograms). However, the physical quantities in the present instance are only frequency and time, and hence only four possibilities exist. The time–time slice of the bipartite chronocyclic tomogram corresponding to state $|\psi\rangle$, is given by,

$$w(t; t') = |\langle t; t'|\psi\rangle|^2, \tag{6}$$

where $|t;\ t'\rangle$ stands for $|t\rangle \otimes |t'\rangle$ in the temporal representation. This is the chronocyclic analogue of (5). The marginal distributions are obtained from (6) as described before.

2.3. Tomographic entanglement indicators

The extent of correlation between the subsystems can be deduced from the tomographic entropies. For instance, for the slice defined in (5), the bipartite tomographic entropy is given by

$$S_{\mathrm{AB}} = -\int_{-\infty}^{\infty} \mathrm{d}x_{\mathrm{a}} \int_{-\infty}^{\infty} \mathrm{d}x_{\mathrm{B}} w(x_{\mathrm{A}}; x_{\mathrm{B}}) \log_2 w(x_{\mathrm{A}}; x_{\mathrm{B}}). \tag{7}$$

The subsystem tomographic entropy is given by

$$S_i = -\int_{-\infty}^{\infty} \mathrm{d}x_i\, w_i(x_i) \log_2 w_i(x_i) \quad (i = \mathrm{A},\mathrm{B}). \tag{8}$$

Signatures of the extent of entanglement can be gleaned from the mutual information [7],

$$\varepsilon_{\rm TEI} = S_{\rm A} + S_{\rm B} - S_{\rm AB}. \tag{9}$$

In the chronocyclic case, analogous definitions of entropies and mutual information hold for any tomographic slice given by (6).

3. Entangled Talbot carpets

For our purposes, we will largely be concerned with the experimental setup proposed in [10] except for the phase shifter used to calculate $I_{\rm D}$. We note that while [10] and the present paper are both concerned with the extent of entanglement of two Talbot carpets, the procedures used are very different. In marked contrast to the procedure for entanglement assessment in [10], we use the tomographic approach to compute the entanglement indicator, namely, $\varepsilon_{\rm tei}$. This can be obtained directly from a single slice of the tomogram provided by the screen in the experimental setup. This approach neither requires a phase shifter in the experimental setup, nor is it concerned with calculating Bell-type inequalities. The purpose of the present work, of course, is to compare the trends in $I_{\rm D}$ reported in [10] with trends in $\varepsilon_{\rm TEI}$, the latter being a very different entanglement indicator.

In the proposed experiment (figure 1), light from a laser source passes through a nonlinear crystal (NLC). Entangled SPDC photon pairs are produced, with a spatial correlation given by

$$R = \frac{\kappa_+^2 - \kappa_-^2}{\kappa_+^2 + \kappa_-^2} = -\frac{\Delta_+^2}{\Delta_-^2}. \tag{10}$$

Here κ_+ is the width of the pump field frequency profile, κ_- is the standard deviation in the phase matching of the two output photons, and

$$\frac{1}{\Delta_\pm^2} = \frac{1}{\kappa_+^2} \pm \frac{1}{\kappa_-^2}. \tag{11}$$

The light is then guided along two different paths A and B using appropriate mirrors. Along path i ($i = {\rm A}, {\rm B}$), a D-slit aperture D_i, a lens L_{1i}, a grating G_i, a lens L_{2i} and a screen Sc_i are placed as shown on the figure. Talbot carpets are seen on each screen, and the extent of entanglement between the two is to be assessed. The slit width in each aperture is δ, and the inter-slit spacing is s. Each grating has slit width σ and period ℓ. The screens are in the x–y plane.

The entangled Talbot state is of the form

$$|\Psi\rangle = \sum_{d_1,d_2=0}^{D-1} C_{d_1,d_2} |d_1\rangle_{\rm A} \otimes |d_2\rangle_{\rm B}, \tag{12}$$

where

$$C_{d_1,d_2} = \mathcal{N} \exp\left\{-\frac{s^2}{4\Delta_+^2}\left(d_1^2 - 2R d_1 d_2 + d_2^2\right)\right\}, \tag{13}$$

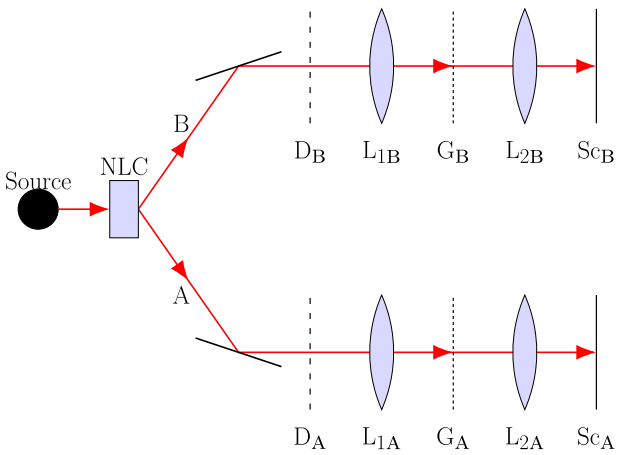

Figure 1. Experimental setup: a pump photon from the laser source is incident on a NLC producing two SPDC photons, each of which passes through a D-slit aperture (D_i), a lens (L_{1i}), a grating (G_i), and another lens (L_{2i}). Sc_i is the detection screen ($i = {\rm a}, {\rm b}$).

where $\mathcal{N}$ is the normalization constant such that $\sum_{d_1,d_2} |C_{d_1,d_2}|^2 = 1$. The basis states are now given by

$$\langle x_i|d\rangle_i = T_d(x_i) = \mathcal{A}_d \sum_{m=-\infty}^{\infty} \times \exp\left\{-\frac{(2\pi m\sigma)^2}{2\ell^2} - \frac{(x_i - ds - m\ell)^2}{4\delta^2}\right\}, \tag{14}$$

where $i = {\rm A}, {\rm B}$ and $\mathcal{A}_d$ is the normalisation constant. It is straightforward to measure the intensity distribution at different points $(x_{\rm A}, x_{\rm B})$ along the x-axis on the two screens. The expression for this distribution can be obtained from $\Psi(x_{\rm A}, x_{\rm B})$ by using (14).

The extent of entanglement has been assessed from $I_{\rm D}$ for different values of the spatial correlation R and the number of slits D [10]. For this purpose, two pairs of local measurements A_1, A_2 (respectively, B_1, B_2) are performed on both A and B. Each of these four measurements has D outcomes with projective operators $\{|f_{\alpha_1}\rangle_{\rm A}\,{}_{\rm A}\langle f_{\alpha_1}|\}$, $\{|f_{\alpha_2}\rangle_{\rm A}\,{}_{\rm A}\langle f_{\alpha_2}|\}$, $\{|g_{\beta_1}\rangle_{\rm B}\,{}_{\rm B}\langle g_{\beta_1}|\}$, and $\{|g_{\beta_2}\rangle_{\rm B}\,{}_{\rm B}\langle g_{\beta_2}|\}$ corresponding to A_1, A_2, B_1, and B_2 respectively. Here

$$|f_{\alpha_j}\rangle_{\rm A} = \frac{1}{\sqrt{D}} \sum_{d=0}^{D-1} {\rm e}^{2\pi i d(f+\alpha_j)/D} |{\rm d}\rangle_{\rm A}, \tag{15}$$

$$|g_{\beta_j}\rangle_{\rm B} = \frac{1}{\sqrt{D}} \sum_{d=0}^{D-1} {\rm e}^{2\pi i d(-g+\beta_j)/D} |{\rm d}\rangle_{\rm B}\ (j = 1, 2) \tag{16}$$

with $\alpha_1 = 0$, $\alpha_2 = 0.5$, $\beta_1 = 0.25$, $\beta_2 = -0.25$ and $f, g = 0, 1, \ldots, D-1$. In what follows, we shall denote the factored product basis $\{|f_{\alpha_i}\rangle_{\rm A} \otimes |g_{\beta_j}\rangle_{\rm B}\}$ by $\{|f_{\alpha_i {\rm A}}; g_{\beta_j {\rm B}}\rangle\}$. (In the tomographic approach that will be outlined later, these phase shifts α_j, β_j ($j = 1, 2$) need not be implemented, and the entanglement indicator can be deduced solely from the original

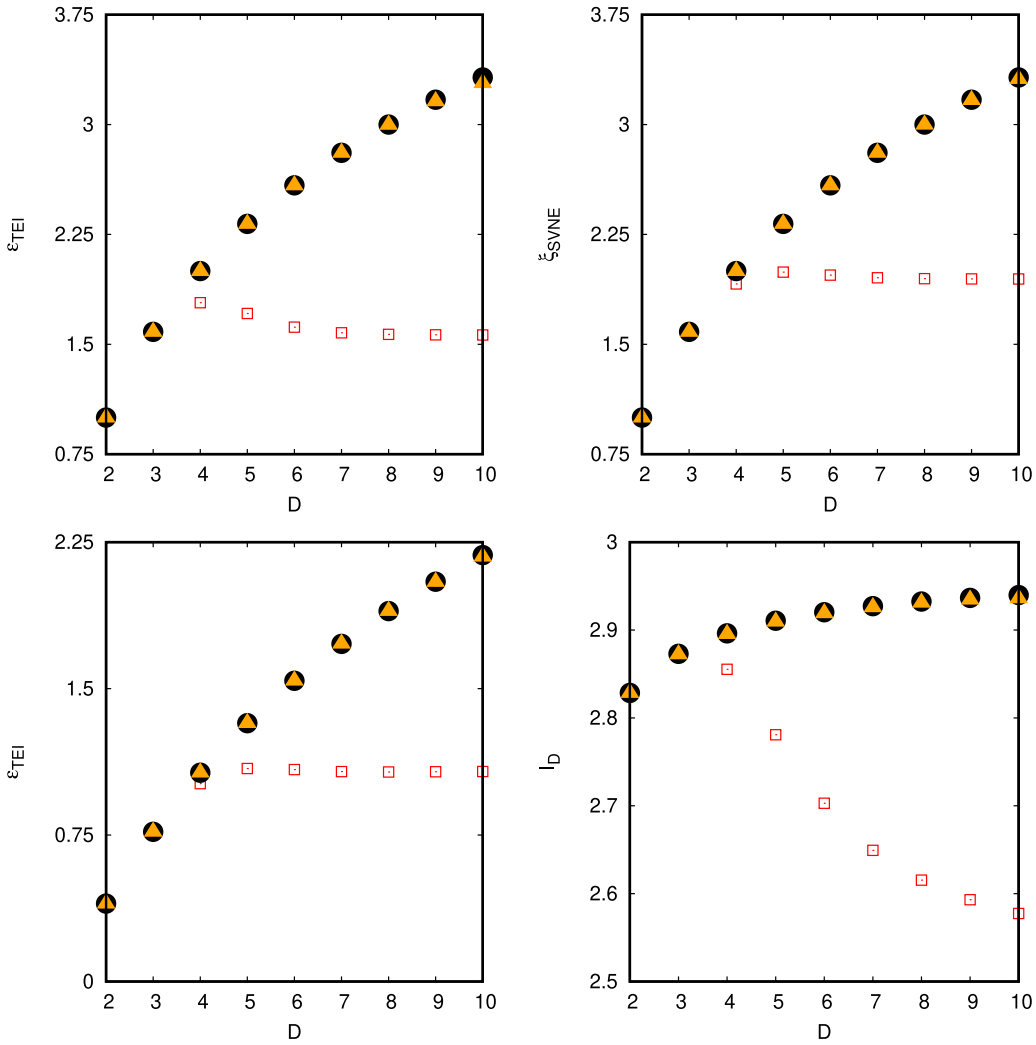

Figure 2. $\varepsilon_{\mathrm{TEI}}$ computed in the $\{|x_{\mathrm{A}}; x_{\mathrm{B}}\rangle\}$ basis (top left), ξ_{SVNE} (top right), $\varepsilon_{\mathrm{tei}}$ computed in the $\{|f_{\alpha_1\mathrm{A}}; g_{\beta_1\mathrm{B}}\rangle\}$ basis (bottom left), and I_{D} (bottom right) vs D for 0.9998 (red), 0.999 98 (orange), and 1 (black). The black and orange curves lie on top of each other. (Color online).

intensity patterns on the screens). It can be seen [37] that for $I_{\mathrm{D}} \leqslant 2$, the states are unentangled. Here,

$$I_{\mathrm{D}} = \sum_{k=0}^{[D/2]-1} \left(1 - \frac{2k}{D-1}\right) J_k, \tag{17}$$

where

$$\begin{aligned} J_k = {} & P(A_1 = B_1 + k) - P(A_1 = B_1 - k - 1) \\ & + P(B_2 = A_1 + k) - P(B_2 = A_1 - k - 1) \\ & + P(B_1 = A_2 + k + 1) - P(B_1 = A_2 - k) \\ & + P(A_2 = B_2 + k) - P(A_2 = B_2 - k - 1) \end{aligned}$$

and

$$P(A_i = B_j + k) = \sum_{p=0}^{D-1} P(A_i = (p+k) \bmod D, B_j = p). \tag{18}$$

The joint probability distribution of the outcomes being $A_i = p$ and $B_j = q$ is denoted by $P(A_i = p, B_j = q)$.

In the tomographic approach (as in the case of I_{D}), we set $\sigma = 0.05\ell$, $\delta = 0.025s$, $\ell = 1$, $s = 1/D$, and $\kappa_+ = 9\ell$ to facilitate comparison. As outlined in section 2, we compute $\varepsilon_{\mathrm{TEI}}$ (see (9)) from the optical tomogram (5). In figure 2, $\varepsilon_{\mathrm{TEI}}$, ξ_{SVNE}, and I_{D} are plotted versus D for various values of R. These values are chosen so as to facilitate comparison with [10]. It is clear that $\varepsilon_{\mathrm{TEI}}$ agrees well with ξ_{SVNE}. Further, $\varepsilon_{\mathrm{TEI}}$ captures the gross features of I_{D}. From figure 2, we see that when $\varepsilon_{\mathrm{TEI}}$ is computed from tomograms corresponding to other basis sets, the results do not change, and that the extent of entanglement significantly increases even with very small changes in R. (For $D = 10$, $\varepsilon_{\mathrm{TEI}} \sim 0.3$ for $R = 0.998$, and ~ 3.32 for $R = 1$ correct to two decimal places).

This feature can be understood by examining the manner in which the subsystem density matrix (in terms of which standard entanglement measures are computed) responds to small changes in R. This is presented in figure 3. We first compare the top left and the bottom left panels in figure 3. These show the subsystem density matrix for $R = 0.998$ and 1 respectively, in the basis set comprising the slits (i.e., where each slit is treated as a basis state). It is evident that the subsystem density matrix

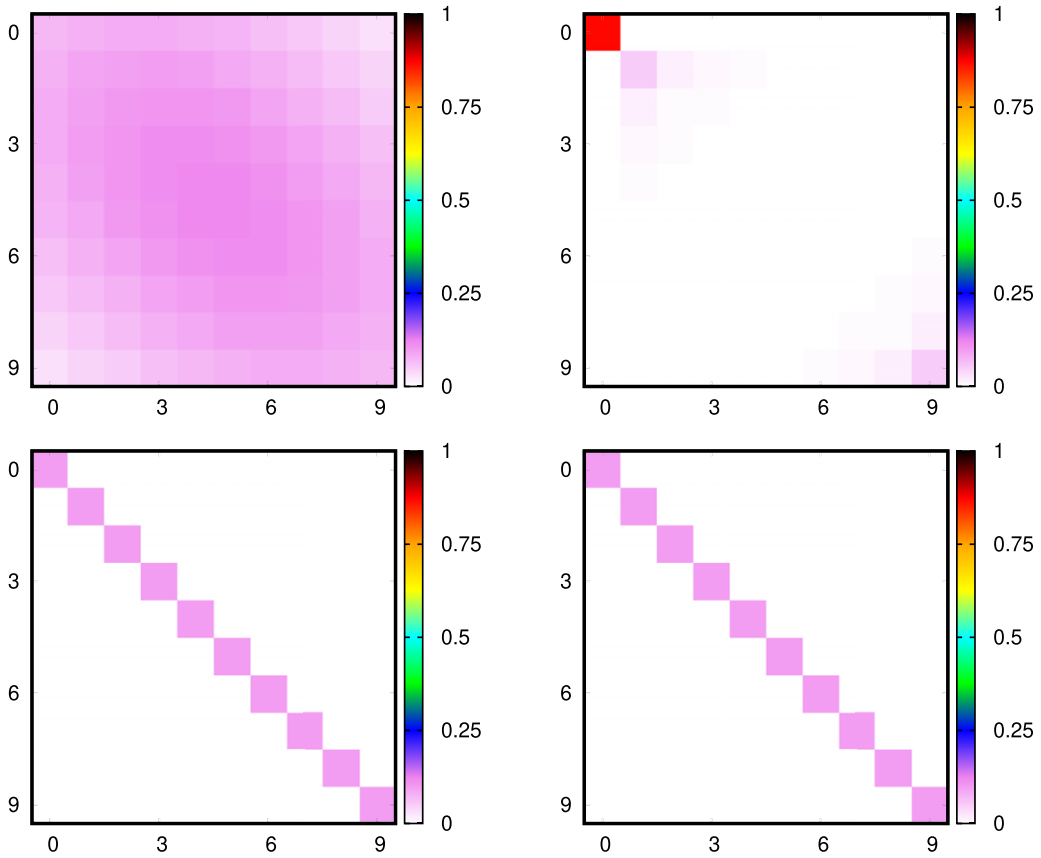

Figure 3. Density matrix corresponding to subsystem A for $R = 0.998$ (top) and $R = 1$ (bottom) in two different basis sets: (left) each slit is treated as a basis state, and (right) $\{|f_{\alpha_1}\rangle_{\rm A}\}$ basis. (Color online).

corresponding to the top left panel has non-zero off-diagonal contributions. In contrast, corresponding to the bottom left panel, the subsystem density matrix is diagonal. For $R = 1$, it is clear from the figure that only the diagonal elements survive, leading to a maximally mixed state. This therefore indicates that the bipartite pure state is maximally entangled for $R = 1$. This is clearly not the case in the top left panel, where the off-diagonal contribution is substantial. We now point out another feature that follows by comparing the top right and the bottom right panels. In both these panels, the subsystem density matrix is given in a different basis which is phase shifted relative to that corresponding to the left panels. (We choose this basis also because it connects with that used in [10] where a phase shifter creates the necessary shift of basis). It is clear from these two panels that a small change in R from 0.998 (top right) to 1 (bottom right) produces a maximally mixed subsystem state. This follows as in the earlier discussion from the diagonal form of the density matrix. A comparison between the bottom right and left panels establishes the basis-independence of the maximally mixed subsystem state for $R = 1$.

4. Biphoton frequency combs

We first recapitulate the salient features of the experiment [18] on two pairs of entangled biphoton states, denoted by $|\Psi_\alpha\rangle$ and $|\Psi_\beta\rangle$, which are frequency combs comprising finite-width peaks. The entangled photons were generated using SPDC. In the setup, the resonant frequency of the cavity is denoted by $\overline{\omega}$, and the pump photons have frequency $\omega_{\rm p}$. If $\omega_{\rm S}$ and $\omega_{\rm I}$ denote the signal and idler frequencies, respectively, and Ω is their difference, it can be seen (appendix A) that $|\Psi_\alpha\rangle$ and $|\Psi_\beta\rangle$ can be expressed as given below.

$$|\Psi_\alpha\rangle = \mathcal{N}_\alpha^{-1/2} \int {\rm d}\omega_{\rm S} \int {\rm d}\omega_{\rm I} f_+(\omega_{\rm S}+\omega_{\rm I}) f_-(\Omega) \times f_{\rm cav}(\omega_{\rm s}) f_{\rm cav}(\omega_{\rm i}) |\omega_{\rm s}\rangle \otimes |\omega_{\rm i}\rangle. \tag{19}$$

Here,

$$f_-(\Omega) = {\rm e}^{-(\Omega-\Omega_0)^2/4(\Delta\Omega)^2}, \tag{20}$$

where Ω_0 and $\Delta\Omega$ are the mean and standard deviation of Ω. $f_{\rm cav}$ is the Gaussian comb

$$f_{\rm cav}(\omega) = \sum_n {\rm e}^{-(\omega-n\overline{\omega})^2/2(\Delta\omega)^2}, \tag{21}$$

where $\Delta\omega$ is the standard deviation of each Gaussian, $\mathcal{N}_\alpha$ is the normalisation constant, and $f_+(\omega_{\rm S}+\omega_{\rm I}) = \delta(\omega_{\rm p}-\omega_{\rm S}-\omega_{\rm I})$. We note that (19) features the product $f_{\rm cav}(\omega_{\rm S}) f_{\rm cav}(\omega_{\rm I})$, where $f_{\rm cav}(\omega)$ is a superposition of Gaussians corresponding to odd and even values of n such that the two are in phase with each other.

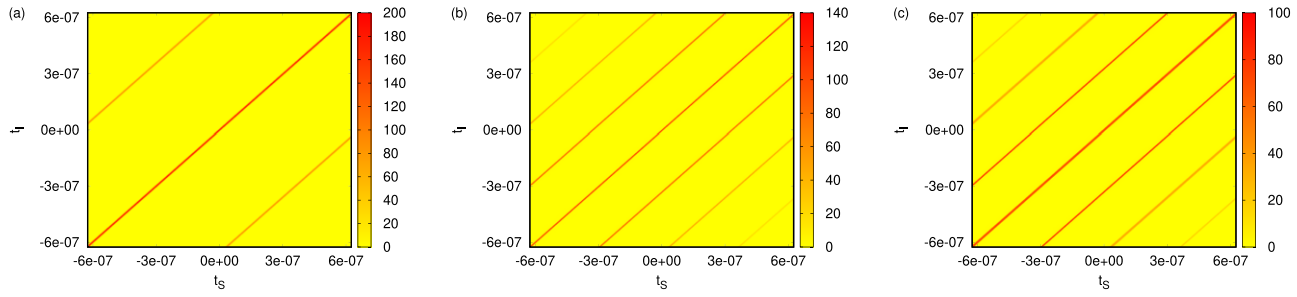

Figure 4. Tomographic time–time slice (a) $w^{\alpha}(t_S;\ t_I)$ and (b) $w^{\beta}(t_S;\ t_I)$ vs t_s and t_i in seconds. (c) Difference $|w^{\alpha}(t_S;\ t_I) - w^{\beta}(t_S;\ t_I)|$ vs t_S and t_I in seconds. (Color online).

The second biphoton state is given by

$$|\Psi_\beta\rangle = \mathcal{N}_\beta^{-1/2} \int \mathrm{d}\omega_S \int \mathrm{d}\omega_I f_+(\omega_S + \omega_I) f_-(\Omega) \times g_{cav}(\omega_S) f_{cav}(\omega_I) |\omega_s\rangle \otimes |\omega_i\rangle, \tag{22}$$

where

$$g_{cav}(\omega) = \sum_n (-1)^n \mathrm{e}^{-(\omega - n\overline{\omega})^2/2(\Delta\omega)^2}. \tag{23}$$

Here, $\mathcal{N}_\beta$ is the normalisation constant. In contrast to $|\Psi_\alpha\rangle$, (22) features the product $g_{cav}(\omega_s) f_{cav}(\omega_i)$, where $g_{cav}(\omega)$ is a superposition of Gaussians corresponding to odd and even n such that the two are out of phase with each other. In [18], the authors address several related issues pertaining to these biphoton frequency combs. The focus is primarily on distinguishing between these entangled states, and further, manipulating them with quantum logic gate operations. Our interest in the present case is only in the former aspect. Whereas in [18] an interferometric setup is used for this purpose, in what follows, we will use the tomographic approach to distinguish between the two biphoton states. Since photon *coincidence* counts were used to experimentally distinguish between the two states, it is reasonable to expect that the time–time slices of the tomograms corresponding to the two biphoton states will capture the difference. The time–time slices are denoted by

$$w^x(t_S; t_I) = \langle t_S; t_I|\Psi_x\rangle\langle\Psi_x|t_S; t_I\rangle, \tag{24}$$

where $(x = \alpha, \beta)$, and $|t_s; t_I\rangle$ stands for $|t_s\rangle \otimes |t_I\rangle$ in the time–time basis.

We work with the parameter values used in reference [18], namely, $\omega_p/(2\pi) = 391.8856$ THz, $\overline{\omega}/(2\pi) = 19.2$ GHz, $\Delta\omega/(2\pi) = 1.92$ GHz, $\Omega_0/(2\pi) = 10.9$ THz, and $\Delta\Omega/(2\pi) = 6$ THz. The time–time slices of the tomograms of $|\Psi_\alpha\rangle$ and $|\Psi_\beta\rangle$ have been obtained by substituting (19) and (22) in turn in (24) and simplifying the resulting expressions (see appendix B).

As expected, $w^{\alpha}(t_S;\ t_I)$ and $w^{\beta}(t_S;\ t_I)$ are distinctly different from each other, as seen in figures 4(a)–(c). This difference arises because $|\Psi_\alpha\rangle$ and $|\Psi_\beta\rangle$ correspond to combs that are clearly displaced with respect to each other, when expressed in the time–time basis.

Next, we calculate the reduced tomograms $w_i^x(t_i)$ corresponding to subsystem i (where $i = S, I$ and $x = \alpha, \beta$) by integrating out the other subsystem. (For instance, $w_s^x(t_s) = \int \mathrm{d}t_i w^x(t_s; t_i)$.) Using these full-system and subsystem chronocyclic tomograms in (7)–(9), we obtain the entanglement indicator ε_{TEI} corresponding to any chosen slice of the chronocyclic tomogram. (For ease of notation, we have dropped the explicit dependence of ε_{TEI} on the choice of both the tomogram slice and the specific state.) In the case of the time–time slice of the tomograms we get, finally, the values $\varepsilon_{TEI} = 6.50$ for the state $|\Psi_\alpha\rangle$, and $\varepsilon_{TEI} = 5.44$ for the state $|\Psi_\beta\rangle$. Thus, ε_{TEI} clearly distinguishes between these two biphoton states. We emphasize that the methods used by us could, in principle, provide an alternative approach to the procedure adopted in the experiment.

5. Concluding remarks

The tomographic entanglement indicator ε_{TEI} proves to be a very useful tool which is also easily computed from the histogram of a relevant measured observable. In the case of the entangled Talbot states, ε_{TEI} computed from the histogram in the position basis, closely mimics the standard entanglement measure ξ_{SVNE}. We emphasize that a single slice suffices to estimate the extent of entanglement, and we do not require the rotated quadratures in this case. In fact, we have shown that ε_{TEI} is better than I_D, the Bell-like-inequality-based indicator. Further, we have unambiguously distinguished between a pair of biphoton states using the entanglement indicator ε_{TEI}. This paper demonstrates alternative procedures using the tomographic approach that are useful and efficient in a variety of experimentally relevant CV systems.

Acknowledgments

We acknowledge useful discussions with P Milman, Laboratoire Matériaux et Phénomènes Quantiques, Université de Paris. SL was supported, in part, by a grant from Mphasis tothe Centre for Quantum Information, Communication, and Computing (CQuICC). B S acknowledges the UK STFC 'Quantum Technologies for Fundamental Physics' program (Grant No. ST/T006404/1) for partial support. We thank the referees for useful suggestions and comments.

Data availability statement

All data that support the findings of this study are included within the article (and any supplementary files).

Appendix A. The biphoton frequency comb states

In section 4, the expressions for the two biphoton states $|\Psi_\alpha\rangle$ and $|\Psi_\beta\rangle$ which are distinguished from each other using tomograms are given in (19) and (22) respectively. For convenience, we give the expressions below.

$$|\Psi_\alpha\rangle = \mathcal{N}_\alpha^{-1/2} \int \mathrm{d}\omega_\mathrm{S} \int \mathrm{d}\omega_\mathrm{I} f_+(\omega_\mathrm{S}+\omega_\mathrm{I}) \times f_-(\Omega) f_\mathrm{cav}(\omega_\mathrm{S}) f_\mathrm{cav}(\omega_\mathrm{I}) |\omega_\mathrm{S}\rangle \otimes |\omega_\mathrm{I}\rangle,$$

where $\mathcal{N}_\alpha$ is the normalisation constant. Here, $f_-(\Omega)$ and $f_\mathrm{cav}(\omega)$ are defined in (20) and (21) respectively. The other biphoton state

$$|\Psi_\beta\rangle = \mathcal{N}_\beta^{-1/2} \int \mathrm{d}\omega_\mathrm{S} \int \mathrm{d}\omega_\mathrm{I} f_+(\omega_\mathrm{S}+\omega_\mathrm{I}) \times f_-(\Omega) g_\mathrm{cav}(\omega_\mathrm{S}) f_\mathrm{cav}(\omega_\mathrm{I}) |\omega_\mathrm{S}\rangle \otimes |\omega_\mathrm{I}\rangle,$$

where $g_\mathrm{cav}(\omega)$ is defined in (23), and $\mathcal{N}_\beta$ is the normalisation constant.

In what follows, we outline the procedure to show that these two states are indeed the two states which were shown to be distinguishable using photon coincidence counts, in the experiment reported in reference [18].

In the experimental setup, the sum of the frequencies of the signal and the idler photons matches the pump frequency, i.e., $(\omega_\mathrm{S}+\omega_\mathrm{I}=\omega_\mathrm{P})$. Hence, as stated in the supplementary material (https://stacks.iop.org/JPB/55/185501/mmedia) of [18], $f_+(\omega_\mathrm{S}+\omega_\mathrm{I})$ can be replaced by $\delta(\omega_\mathrm{S}+\omega_\mathrm{I}-\omega_\mathrm{P})$. Integrating over the variable $\Omega_+(=\omega_\mathrm{s}+\omega_\mathrm{i})$, appropriately changing the integration variables, noting that $\Omega=\omega_\mathrm{s}-\omega_\mathrm{i}$, and dropping the normalisation constant, we get

$$|\Psi_\alpha\rangle = \int \mathrm{d}\Omega f_-(\Omega) f_\mathrm{cav}(\omega_\mathrm{S}) f_\mathrm{cav}(\omega_\mathrm{I}) |\omega_\mathrm{S}\rangle \otimes |\omega_\mathrm{I}\rangle. \quad (A.1)$$

This can be identified as one of the states considered in the experiment, namely, the expression (B19) in [18], on changing the notation from Ω, ω_S, ω_I in (A.1) to ω_-, ω_S, ω_I respectively.

We now proceed to establish that the other biphoton state $|\Psi_\beta\rangle$ considered by us, is the same as the state $|\psi'\rangle$ $(=C' Z_{t_\mathrm{S}} |\widetilde{+}\rangle_{\omega_\mathrm{S}} \otimes |\widetilde{+}\rangle_{\omega_\mathrm{I}})$ defined in [18]. Here, $C'|t_\mathrm{S};\ t_\mathrm{I}\rangle = |t_\mathrm{S}+t_\mathrm{I};\ t_\mathrm{S}-t_\mathrm{I}\rangle$ where, for instance, $|t_\mathrm{S}\rangle \otimes |t_\mathrm{I}\rangle$ is denoted by $|t_\mathrm{S};\ t_\mathrm{I}\rangle$ with t_S and t_I being the time variables associated with the signal and the idler photons respectively, and $Z_{t_\mathrm{s}} |\widetilde{+}\rangle_{\omega_\mathrm{s}} = |\widetilde{-}\rangle_{\omega_\mathrm{s}}$. It is convenient to express $|\widetilde{+}\rangle_{\omega_x}$ and $|\widetilde{-}\rangle_{\omega_x}$ $(x=\mathrm{S,I})$ as

$$|\widetilde{+}\rangle_{\omega_x} = \int \mathrm{d}\omega_x \int \mathrm{d}t_x \ \exp\left(-\frac{t_x^2}{2\kappa_x^2} - \frac{\omega_x^2}{2(\Delta\omega)^2}\right) \sum_n \mathrm{e}^{\mathrm{i}(\omega_x+n\bar{\omega})t_x} |\omega_x+n\bar{\omega}\rangle, \quad (A.2)$$

and

$$|\widetilde{-}\rangle_{\omega_x} = \int \mathrm{d}\omega_x \int \mathrm{d}t_x \ \exp\left(-\frac{t_x^2}{2\kappa_x^2} - \frac{\omega_x^2}{2(\Delta\omega)^2}\right) \sum_n (-1)^n \mathrm{e}^{\mathrm{i}(\omega_x+n\bar{\omega})t_x} |\omega_x+n\bar{\omega}\rangle. \quad (A.3)$$

These expressions follow from the properties of the displacement operator, and the expressions (B1), (B2) and (B7) given in [18]. Here, $\kappa_x (x=\mathrm{S,I})$ is the standard deviation in t_x. It follows from (A.2) and (A.3) that

$$|\psi'\rangle = \int \mathrm{d}t \int \mathrm{d}t' \int \mathrm{d}\omega \int \mathrm{d}\omega' \times \exp\left(-\frac{t^2(\Delta\omega_p)^2 + t'^2(\Delta\Omega)^2}{2} - \frac{\omega^2+\omega'^2}{2(\Delta\omega)^2}\right) \sum_{n,m} (-1)^n \mathrm{e}^{\mathrm{i}(n\bar{\omega}+\omega)(t+t')} \mathrm{e}^{\mathrm{i}(m\bar{\omega}+\omega')(t-t')} |n\bar{\omega}+\omega\rangle \times \otimes |m\bar{\omega}+\omega'\rangle, \quad (A.4)$$

where $\Delta\omega_\mathrm{P}$ is the standard deviation in ω_P. Integrating over the time variables t and t', writing $(\omega_\mathrm{S}=n\bar{\omega}+\omega)$, $(\omega_\mathrm{I}=m\bar{\omega}+\omega')$ where n, m are integers, and using the fact that f_+ is a Gaussian function with a standard deviation $\Delta\omega_\mathrm{P}$ $(\Delta\omega_\mathrm{P} \ll \Delta\Omega)$, it is straightforward to see that (A.4) can be expressed as $|\Psi_\beta\rangle$ in (22), unnormalised.

Appendix B. Expressions for the chronocyclic tomograms

We are interested in the time–time slice of the tomograms corresponding to $|\Psi_\alpha\rangle$ (19) and $|\Psi_\beta\rangle$ (22). As a first step, we calculate the explicit expressions for the states $|\Psi_\alpha\rangle$ and $|\Psi_\beta\rangle$ in the Fourier transform basis (i.e., time–time basis) using $f_+(\omega_\mathrm{S}+\omega_\mathrm{I}) = \delta(\omega_\mathrm{S}+\omega_\mathrm{I}-\omega_\mathrm{P})$ in (19) and (22). The biphoton state $|\Psi_\alpha\rangle$ in the time–time basis is given by

$$|\Psi_\alpha\rangle = \frac{1}{\sqrt{\mathcal{M}_\alpha \tau_\mathrm{P}}} \int \mathrm{d}t_\mathrm{S} \int \mathrm{d}t_\mathrm{I} \times \exp\left(-\frac{(t_\mathrm{I}-t_\mathrm{S})^2 (\Delta\omega)^2 (\Delta\Omega)^2}{4\left((\Delta\omega)^2+(\Delta\Omega)^2\right)}\right) \times [\mathcal{F}(t_\mathrm{I}-t_\mathrm{S})]^2 |t_\mathrm{s};\ t_\mathrm{I}\rangle, \quad (B.5)$$

and the time–time slice $w^\alpha(t_\mathrm{S};\ t_\mathrm{I})$ corresponding to $|\Psi_\alpha\rangle$ is

$$w^\alpha(t_\mathrm{S};t_\mathrm{I}) = \frac{1}{\mathcal{M}_\alpha \tau_\mathrm{P}} \times \exp\left(-\frac{(t_\mathrm{I}-t_\mathrm{S})^2 (\Delta\omega)^2 (\Delta\Omega)^2}{2\left((\Delta\omega)^2+(\Delta\Omega)^2\right)}\right) |\mathcal{F}(t_\mathrm{I}-t_\mathrm{S})|^4,$$

where $\tau_\mathrm{p} = 1$ s (introduced for dimensional purposes),

$$\mathcal{F}(t_\mathrm{I}-t_\mathrm{S}) = \sum_n \exp\left(\frac{i(t_\mathrm{I}-t_\mathrm{S})\, n\, \bar{\omega} (\Delta\Omega)^2}{2((\Delta\omega)^2+(\Delta\Omega)^2)}\right),$$

and the normalisation constant is

$$\mathcal{M}_\alpha = \frac{\pi}{\mu_0} \sum_{m,n,m',n'} \exp\left(-\frac{(n-n'+m'-m)^2\,\overline{\omega}^2\,(\Delta\Omega)^2}{2\,(\Delta\omega)^2\,((\Delta\omega)^2+(\Delta\Omega)^2)}\right), \tag{B.6}$$

where $\mu_0 = \left(\frac{\pi(\Delta\Omega)^2(\Delta\omega)^2}{2((\Delta\Omega)^2+(\Delta\omega)^2)}\right)^{1/2}$.

Similarly, the other biphoton state $|\Psi_\beta\rangle$ in the time–time basis is given by

$$\begin{aligned}|\Psi_\beta\rangle = \frac{1}{\sqrt{\mathcal{M}_\beta \tau_{\rm P}}} \int {\rm d}t_{\rm S} \int {\rm d}t_{\rm I} \\ \times \exp\left(-\frac{(t_{\rm I}-t_{\rm S})^2\,(\Delta\omega)^2\,(\Delta\Omega)^2}{4\,((\Delta\omega)^2+(\Delta\Omega)^2)}\right) \\ \times \mathcal{G}(t_{\rm I}-t_{\rm S})\,\mathcal{F}(t_{\rm I}-t_{\rm S})|t_{\rm S};t_{\rm I}\rangle,\end{aligned} \tag{B.7}$$

and the time–time slice corresponding to $|\Psi_\beta\rangle$ is

$$\begin{aligned}w^\beta(t_{\rm S};t_{\rm I}) = \frac{1}{\mathcal{M}_\beta \tau_{\rm P}} \exp\left(-\frac{(t_{\rm I}-t_{\rm S})^2\,(\Delta\omega)^2\,(\Delta\Omega)^2}{2\,((\Delta\omega)^2+(\Delta\Omega)^2)}\right) \\ \times |\mathcal{G}(t_{\rm I}-t_{\rm S})\,\mathcal{F}(t_{\rm I}-t_{\rm S})|^2,\end{aligned}$$

where,

$$\mathcal{G}(t_{\rm I}-t_{\rm S}) = \sum_n (-1)^n \exp\left(\frac{i(t_{\rm I}-t_{\rm S})\,n\,\bar{\omega}(\Delta\Omega)^2}{2((\Delta\omega)^2+(\Delta\Omega)^2)}\right),$$

and the normalisation constant $\mathcal{M}_\beta$ is essentially the same as $\mathcal{M}_\alpha$ with an extra factor of $(-1)^{n+n'}$ within the summation in (B.6).

ORCID iDs

B Sharmila https://orcid.org/0000-0002-3947-3628

References

[1] Toninelli E, Ndagano B, Vallés A, Sephton B, Nape I, Ambrosio A, Capasso F, Padgett M J and Forbes A 2019 *Adv. Opt. Photon.* **11** 67–134

[2] Bantysh B I, Bogdanov Y I, Bogdanova N A and Kuznetsov Y A 2020 *Laser Phys. Lett.* **17** 035205

[3] Keith A C, Baldwin C H, Glancy S and Knill E 2018 *Phys. Rev.* A **98** 042318

[4] Lv D, An S, Um M, Zhang J, Zhang J N, Kim M S and Kim K 2017 *Phys. Rev.* A **95** 043813

[5] Rohith M and Sudheesh C 2016 *J. Opt. Soc. Am.* B **33** 126–33

[6] Sharmila B, Lakshmibala S and Balakrishnan V 2020 *J. Phys. B: At. Mol. Opt. Phys.* **53** 245502

[7] Sharmila B, Saumitran K, Lakshmibala S and Balakrishnan V 2017 *J. Phys. B: At. Mol. Opt. Phys.* **50** 045501

[8] Sharmila B, Lakshmibala S and Balakrishnan V 2019 *Quantum Inf. Process.* **18** 236

[9] Sharmila B, Lakshmibala S and Balakrishnan V 2020 *Quantum Inf. Process.* **19** 127

[10] Barros M R, Ketterer A, Farías O J and Walborn S P 2017 *Phys. Rev.* A **95** 042311

[11] Talbot H F 1836 *London, Edinburgh Dublin Phil. Mag. J. Sci.* **9** 401–7

[12] Song X B, Wang H B, Xiong J, Wang K, Zhang X, Luo K H and Wu L A 2011 *Phys. Rev. Lett.* **107** 033902

[13] Schwarz S *et al* 2020 *Phys. Rev.* A **101** 043815

[14] Azizi B, Amini Sabegh Z, Mahmoudi M and Rasouli S 2021 *Sci. Rep.* **11** 6827

[15] Farías O J, de Melo F, Milman P and Walborn S P 2015 *Phys. Rev.* A **91** 062328

[16] Arora A S and Asadian A 2015 *Phys. Rev.* A **92** 062107

[17] Hall L A, Yessenov M, Ponomarenko S A and Abouraddy A F 2021 *APL Photon.* **6** 056105

[18] Fabre N *et al* 2020 *Phys. Rev.* A **102** 012607

[19] Chang K-C *et al* 2021 *npj Quantum Inf.* **7** 48

[20] Yamazaki T, Ikuta R, Kobayashi T, Miki S, China F, Terai H, Imoto N and Yamamoto T 2022 *Sci. Rep.* **12** 8964

[21] Ketterer A, Keller A, Walborn S P, Coudreau T and Milman P 2016 *Phys. Rev.* A **94** 022325

[22] Fabre N and Felicetti S 2021 *Phys. Rev.* A **104** 022208

[23] Fabre N 2022 *J. Mod. Optic.* **69** 653–64

[24] Fabre N 2022 *Phys. Rev.* A **105** 053716

[25] Ducci S, Milman P and Diamanti E 2021 *Photoniques* **107** 28–34

[26] Boucher G, Douce T, Bresteau D, Walborn S P, Keller A, Coudreau T, Ducci S and Milman P 2015 *Phys. Rev.* A **92** 023804

[27] Fabre N, Keller A and Milman P 2022 *Phys. Rev.* A **105** 052429

[28] Francesconi S, Raymond A, Fabre N, Lemaître A, Amanti M I, Milman P, Baboux F and Ducci S 2021 *ACS Photon.* **8** 2764–9

[29] Fabre N *et al* 2020 *Phys. Rev.* A **102** 023710

[30] Francesconi S, Baboux F, Raymond A, Fabre N, Boucher G, Lemaître A, Milman P, Amanti M I and Ducci S 2020 *Optica* **7** 316–22

[31] Sawada K and Walborn S P 2018 *J. Opt.* **20** 075201

[32] Vogel K and Risken H 1989 *Phys. Rev.* A **40** 2847–9

[33] Lvovsky A I and Raymer M G 2009 *Rev. Mod. Phys.* **81** 299–332

[34] Ibort A, Man'ko V I, Marmo G, Simoni A and Ventriglia F 2009 *Phys. Scr.* **79** 065013

[35] Paye J 1992 *IEEE J. Quantum Electron.* **28** 2262–73

[36] Beck M, Walmsley I A, Wong V and Raymer M G 1993 *Opt. Lett.* **18** 2041–3

[37] Collins D, Gisin N, Linden N, Massar S and Popescu S 2002 *Phys. Rev. Lett.* **88** 040404